Engineering Structures 326 (2025) 119491

Contents lists available at ScienceDirect

Engineering Structures

journal homepage: www.elsevier.com/locate/engstruct

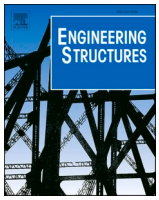

Cumulative effects of cracking in monoblock multipurpose precast concrete sleepers on railway tracks

Jesús Donaire-Ávila *, Javier F. Aceituno, Fernando Suárez

Department of Mechanical and Mining Engineering, University of Jaén, Avda. Universidad, 23700 Linares, Jaén, Spain

ARTICLE INFO

Keywords:
Precast concrete sleepers
Polyamide dowels
Cracking
Thermo-mechanical loads
Installation
Railway track

ABSTRACT

This work addresses the phenomenon of cracking in multipurpose precast monoblock concrete sleepers by examining the entire process from fabrication to final installation on railway tracks. This includes stages such as manufacturing, stockpiling, track installation for rail neutralization, and eventually fastening the rails to the sleepers. A nonlinear numerical model, which is experimentally validated, is used to analyze this effect. Also, thermal and mechanical actions are considered at each stage of the process. Accordingly, different types of polymeric dowels and concrete aggregates—siliceous and carbonate—are evaluated to assess their impact on cracking. The results indicate that the thermal expansion capacity and elastic stiffness of the dowels, as well as the outdoor temperatures during fabrication, stockpiling, and installation, play critical roles in the cracking process. Sleepers made with carbonate aggregate, stiff-expansive dowels, fabricated in cold environments, and installed in hot conditions are particularly prone to severe cracking. Consequently, these conditions should be avoided to minimize cracking in multipurpose sleepers.

1. Introduction

Railway sleepers are fundamental structural elements that ensure the stability, safety, and longevity of railway tracks. They support the rails, redistribute axial forces, maintain rail gauge, and ensure the proper distribution of loads from the rails to the ballast [1,2]. Sleepers transfer and distribute wheel loads from the rail to the ballast bed, supporting the entire railway structure [3]. They also anchor the fastening system, restrict rail movement in various directions, and help maintain track geometry within acceptable limits [4]. The importance of railway sleepers is highlighted by their role in preventing track component degradation, which could lead to derailments and increased maintenance costs [5]. They are vital for maintaining the structural integrity of the railway system, ensuring track alignment, gauge, and overall stability.

Due to the substantial number of sleepers installed within railway infrastructure, maximizing their durability to reduce maintenance cost and environmental impact is the subject of extensive research within the literature. In this sense, the use of recycled rubber products such as under-sleeper pads, under-ballast mats, recycled tire cells, and granulated rubber has been introduced to improve the performance of railway tracks [6–8], which also leads to eco-friendly production methods in their sustainability and serviceability [9]. These materials contribute to better load distribution, reduced track settlement, and improved track resilience, all of which are essential factors for ensuring the longevity of railway sleepers and tracks.

One of the main challenges that directly affects the durability of railroad sleepers is the presence and propagation of cracks, leading to their replacement and subsequent economic and environmental impact [10]. In this regard, there is significant variability in the causes contributing to the presence and growth of cracks, such as dynamic effects from train passage [11,12], climatological influences like cyclic variations in humidity [13] and temperature [14], or even aspects related to the geometric design of sleepers and the positioning and material-based of dowels for rail screws [15,16].

In addition to the aforementioned causes of crack propagation, the combined effect of tightening torque during on-site installation and significant temperature fluctuations during sleeper storage before installation requires special attention (Fig. 1). Derkowski et al. [17] found that excessively tight rail anchors can increase friction resistance, leading to greater force transmission, and recommend adjusting torque values to restore elastic properties. Zeng et al. [18] highlighted that temperature differences can cause cracks in track structures, particularly at the corners of sleeper blocks. Donaire et al. [16] conducted a prior study to analyze the influence of geometry and material types used in the

* Corresponding author.
E-mail addresses: jdonaire@ujaen.es (J. Donaire-Ávila), jaceitun@ujaen.es (J.F. Aceituno), fsuarez@ujaen.es (F. Suárez).

https://doi.org/10.1016/j.engstruct.2024.119491
Received 18 July 2024; Received in revised form 4 November 2024; Accepted 9 December 2024
Available online 19 December 2024

Nomenclature

f_c	Concrete stress under compression
f_{cp}	Concrete peak stress under compression
ε_c	Concrete strain under compression
ε_{cp}	Concrete strain at peak stress under compression
ε_{t1}	Principal concrete tensile strain
σ_{t1}	Principal concrete tensile stress
n	Adjusting parameter for the pre-peak behavior of concrete under compression
k	Adjusting parameter for the post-peak behavior of concrete under compression
f_t	Concrete stress under tension
f_{tp}	Concrete peak stress under tension
ε_t	Concrete strain under tension
ε_{tp}	Concrete strain at peak stress under tension
s_{cr1}	Distance used to compute the crack width
w	Crack width
T	Tightening torque
K	Torque coefficient
N_s	Axial force due to the tightening torque
$\phi_{M,s}$	Major diameter of the screw thread
$v_{s,clip}$	Vertical displacement of the clip at the screw axis
$v_{e,clip}$	Vertical displacement of the clip at the end of the clip in contact with the screw
θ, λ	Angles related to the dowel geometry
σ_r	Radial component of the stress vector induced by the tightening torque
S_{tot}	Total area of the dowel's helicoidal surface
$\sigma_{r,eq}$	Equivalent radial compression stress in the 2D-FEM model
l_d	Length of the dowel
$\phi_{M,d}$	Major diameter of the dowel
R_{Torque}	Reaction force of one-half of the dowel-screw set at the sleeper`s longitudinal axis
$\Delta T_{eq,s}$	Equivalent temperature increment applied to the screw
$\Delta T_{eq,d}$	Equivalent temperature increment applied to the dowel
α_s	Screw thermal expansion coefficient
α_d	Dowel thermal expansion coefficient
T_n	Neutralization temperature
T_{rail}	Rail temperature
T_f	Fabrication temperature
ΔT_s	Temperature increment at stockpiling over the fabrication temperature
T_i	Installation temperature
ΔT_i	Temperature increment at installation over the fabrication temperature
T_r	Required tightening torque
E	Elastic modulus
ν	Poisson's ratio
α	Thermal expansion coefficient
t	Dowel thickness
$\Delta T_{eq,s2}$	Equivalent temperature increment at the screw required to induce T_r at dowel-screw set No. 2
$\Delta T_{eq,d2}$	Equivalent temperature increment at the dowel required to induce T_r at dowel-screw set No. 2
$\Delta T_{eq,s1}$	Equivalent temperature increment at the screw required to induce T_r at dowel-screw set No. 1
$\Delta T_{eq,d1}$	Equivalent temperature increment at the dowel required to induce T_r at dowel-screw set No. 1

Fig. 1. Cracking in monoblock multipurpose concrete sleepers installed on the railway track.

fabrication of multipurpose concrete sleepers subjected to temperature increments before their installation on the railway track. They demonstrated that when dowels are made of materials with high elastic modulus and high thermal expansion coefficients, the induced crack opening due to temperature increments can lead to significant crack propagation in multipurpose concrete sleepers.

Among the causes of crack propagation in railway sleepers described above, this work focuses on the cumulative effects by the combination of factors not yet analyzed in the literature, which can be crucial for the durability of railway sleepers: the influence of the tightening torque combined with previous temperature variations of the sleepers during stockpiling and in situ installation. To this end, this work builds on the findings of the previous research [16] by analyzing crack growth evolution in multipurpose concrete sleepers during on-site installation, considering the prestressed load, temperature variations during sleeper stockpiling and their installation on the track and, eventually, the tightening torque for both different types of concrete materials and different polymeric—polyamide—dowels used in the anchor system. A nonlinear numerical model is used accordingly, taking into account thermal and mechanical actions at all stages to obtain the resulting crack pattern.

2. Benchmark multipurpose sleeper and track installation

Monoblock multipurpose prestressed concrete sleepers, herein MMPC sleepers, allow fastening the rails for both the Iberian and the Standard gauges, 1668 mm and 1435 mm, respectively (Fig. 2). They are widely used in Spain for both conventional and high-speed railway tracks.

The benchmark MMPC sleeper used in this study is prefabricated and made by the following components: (i) high strength concrete—60 MPa in this case; (ii) four prestressed bars; (iii) four polymeric dowels at each end of the sleeper, facilitating a direct fastening system—SKL type—that secures the rails for both potential track gauges. More specifically, this study considered polyamide dowels with and without fiber reinforcement. Furthermore, the SKL fastening system combines a zinc-plated screw spike—herein screw, a zinc-plated washer, a painted rail elastic clip SKL-1 and the dowel. The elastic clip is supported in a polymeric guide plate—embedded, in turn, in the upper part of the MMPC—and also secures the rail track base (Fig. 2b).

MMPC sleepers undergo various actions during fabrication, stockpiling and installation on railway tracks. During the fabrication process, the concrete is poured in a metal formwork system where the prestressed wires are secured. It is then transferred to a heating and curing chamber for the gradual development of the concrete's strength. Once the sleepers

Fig. 2. Set up of rails and MMPC sleepers for the Iberian gauge (a) by using the SKL fastening system (b).

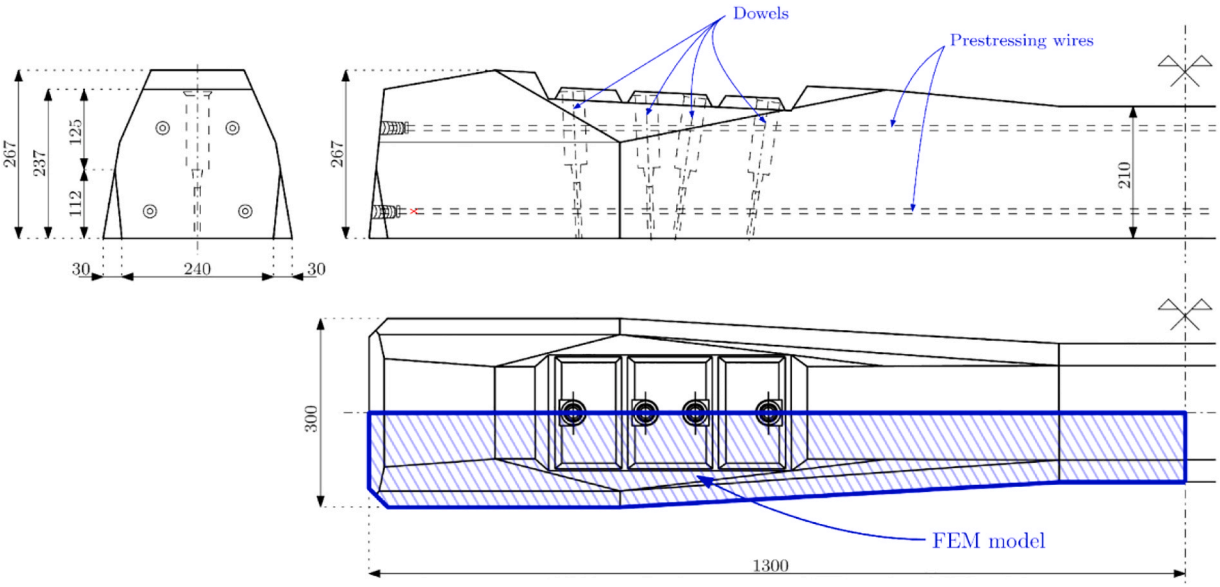

Fig. 3. Shape and dimensions of one half of a sleeper. Dimensions are expressed in mm.

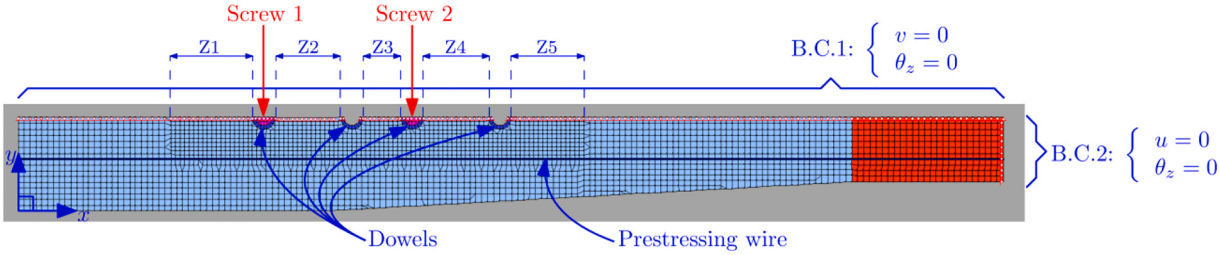

Fig. 4. Parts and boundary conditions of the finite element model (Vector2).

are removed from the chamber at ambient temperature, the prestressing force is applied and the fastening system is set-up with a slight tightening torque. The sleepers are then stockpiled outdoors until they are transported to the construction site and placed alongside the track, experiencing temperature variations during this time. After ballast placement, the sleepers are installed. The installation of continuous welded rails requires specific outdoor conditions, particularly regarding the ambient temperature. This technique involves neutralizing the railway track to de-stress the rails before installation. Rails must be fastened to the sleepers at or below the neutralization temperature, T_n, to prevent buckling or track cutting. The neutralization temperature is estimated as $T_n = (T_{\max} + T_{\min})/2 + 5\,^{\circ}\mathrm{C}$, where T_{max} and T_{min} are the highest and the lowest expected ambient temperatures in the region [19]. Rails can be neutralized through the solar heating method, where they are naturally heated until the ambient temperature matches T_n. Alternatively, when the temperature is below, rails can be neutralized by elongation to the neutralization length—length of the rails under T_n—through thermal or mechanical methods. In Spain, T_n ranges between 24 °C to 37 °C, depending on the region [19]. The maximum allowed absolute difference between the rail temperature, T_{rail}, and T_n is 47 °C [19], meaning that T_{rail} could reach up to 84 °C.

3. Numerical model of the MMPC sleeper

To analyze the evolution of cracking in railway sleepers under temperature variation and the tightening torque for rail fastening, a

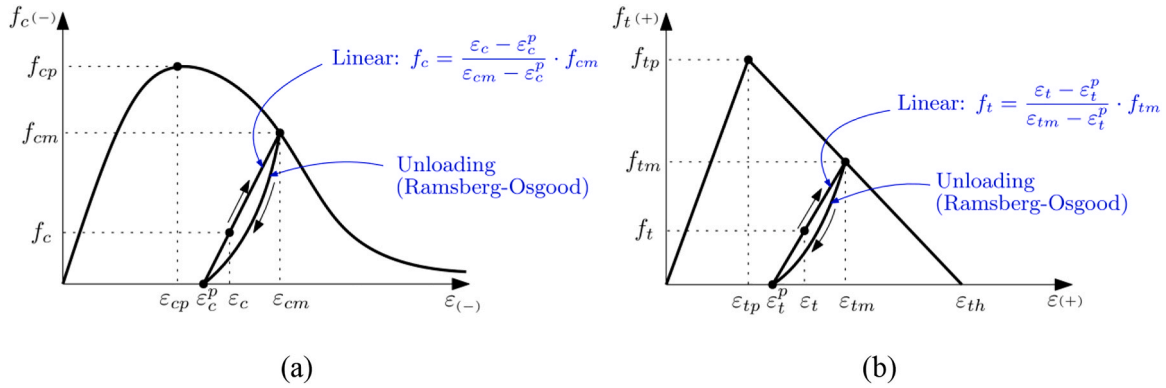

Fig. 5. Constitutive model for the high strength concrete: (a) compression; (b) tension.

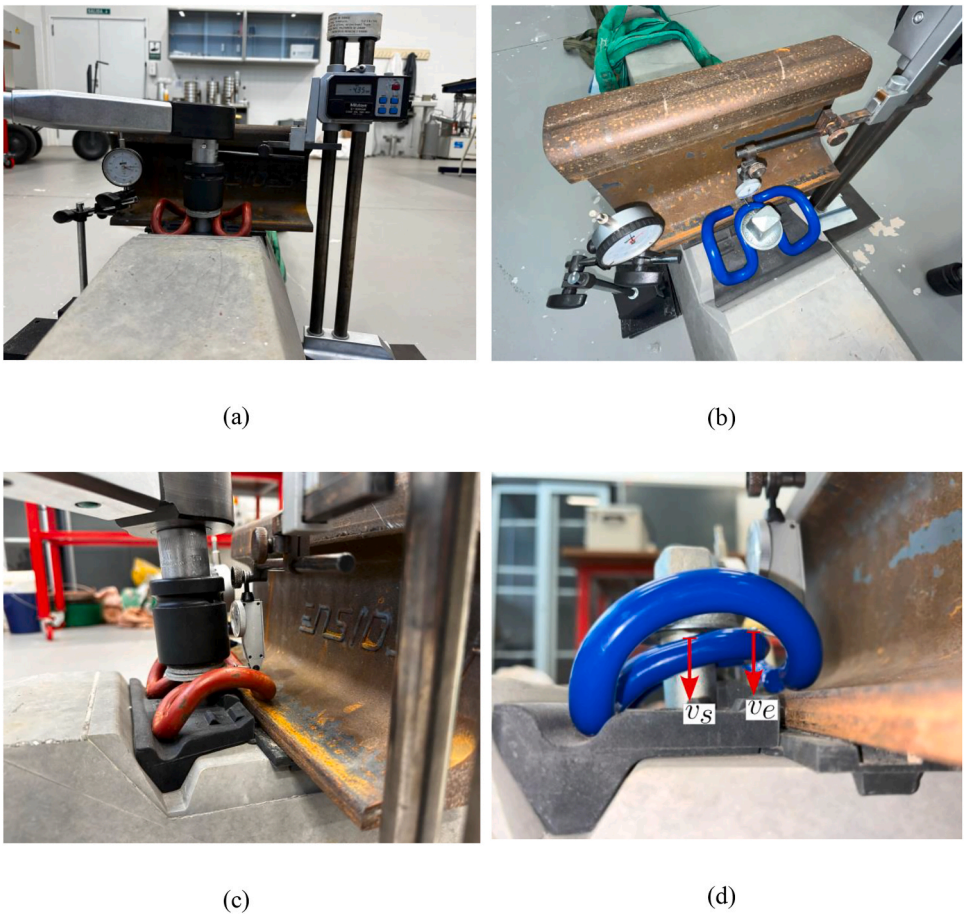

Fig. 6. Experimental test to estimate the torque coefficient of the screw in the SKL fastening system: Set-U (a and c) and Set-Un (b and d).

finite element model was developed using Vector2 software [20]. Fig. 3 shows the geometry, main dimensions, and key components of the railway sleeper, including the prestressing wires and dowels used for screw placement in the rail fastening process.

The model is a plane stress bidimensional model—herein 2D-FEM—that, taking advantage of the double symmetry of the problem, represents one quarter of the sleeper (blue shaded region in Fig. 3), with the following main elements shown in Fig. 4:

- Boundary conditions (B.C.) reproduce the double symmetry of the problem. Nodes at the top boundary can only move in the x axis direction (B.C.1), while nodes at the right boundary can only move in the y direction (B.C.2).
- Concrete elements in the light blue region in Fig. 4 have a thickness of 230 mm while elements in the red region have a thickness of 210 mm.
- Concrete cracking is reproduced using a smeared crack formulation, detailed in Section 3.1. Two types of concrete with differing behavior under temperature variation, will be considered based on the aggregate type used in the mix.
- Prestressing force is represented by truss elements following the prestressing path. These truss elements have a circular section with a diameter of 10.50 mm and are connected to the surrounding 2D elements at the shared nodes. The prestressing force corresponds to one half of the total one, reaching 225 kN.

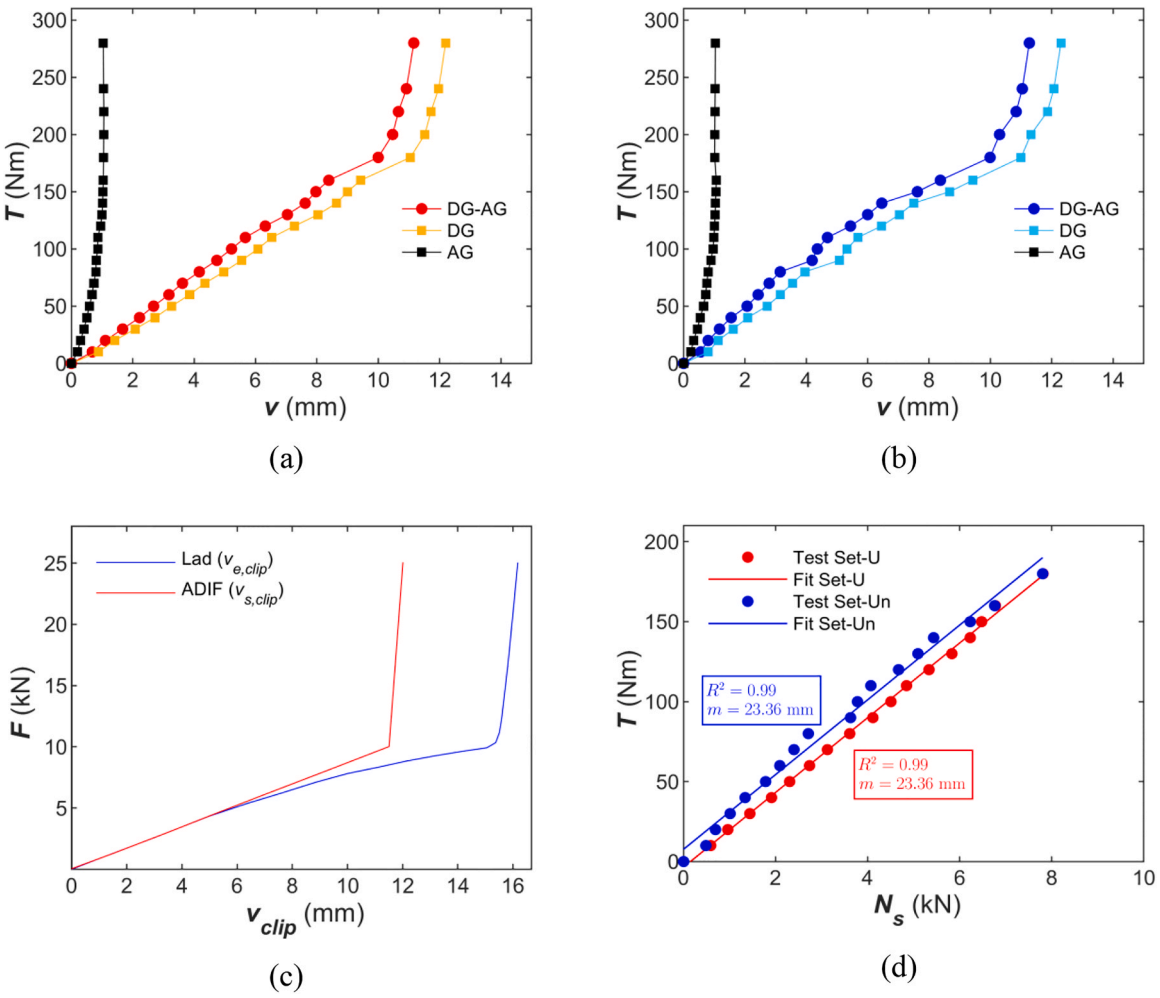

Fig. 7. Structural response of the fastening systems: *T*-*v* curves obtained from the experimental test for Set-U (a) and Set-Un (b); (c) N_s-*v* curves proposed in the literature [26,27]; (d) *T*-N_s relationships.

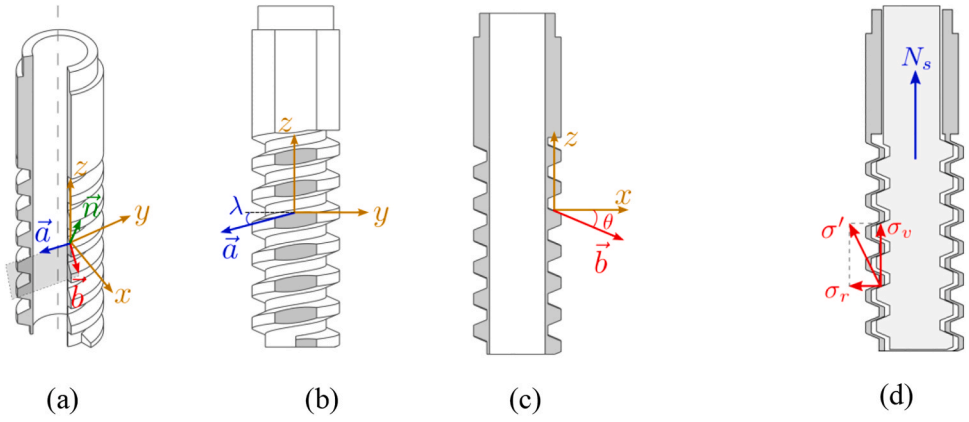

Fig. 8. Definition of the tangent plane and stresses generated by the dowel-screw set (sectioned areas are drawn in gray): (a) tangent plane to the thread of a dowel; (b) Z-Y section; (c) Z-X section; (d) stresses transmitted to the concrete.

- Dowels are modeled as 120 mm thick elastic elements around the holes where rail fastening screws are placed (blue elements in Fig. 4). As analyzed in [16], these dowels can exhibit varying mechanical properties under temperature changes, significantly affecting crack evolution. Two types of dowels will be considered in this study. Given that the analyzed sleeper is multipurpose, it has four dowels at each end, with only two used for rail fastening simultaneously. Therefore, the simulation includes two empty holes and two holes containing screws, a crucial factor during temperature variations. Screws are modeled as 120 mm thick elements, like the dowels, and are placed in the first and third dowel holes (Iberian gauge), counting from the left in Fig. 4 (magenta elements).

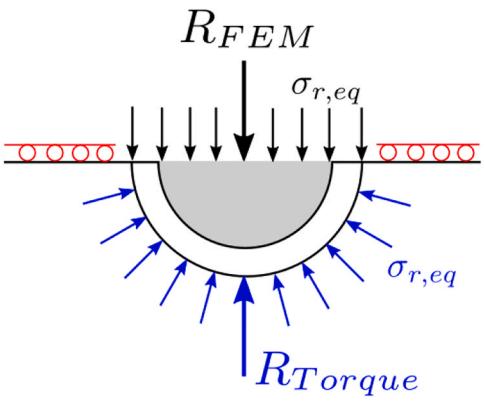

Fig. 9. Stress field in the dowel-screw set of the 2D-FEM under tightening torque (plan view near the symmetry axis).

- The prestressing wire, dowels and screws are all modeled as elastic materials. In all cases, the elastic limit is never reached in the analysis.
- To clearly describe the cracking process, distinct regions are identified along the B.C.1 symmetry axis. These five zones, labeled Z1 to Z5 (Fig. 4), correspond to areas between and near the dowels, which are the primary regions of crack evolution in the sleeper.

This model, experimentally validated in [16], is used here to analyze the influence of several factors on the problem, including the fastening torque, which will be described in detail later.

3.1. Concrete material model

Under compression, the stress-strain backbone curve of concrete becomes nonlinear when close to the maximum bearing capacity. To simulate this, the model uses the formulation proposed by Popovics [21], but modified by Thorenfeldt et al. to adapt it for high-strength concrete [22], which is described by Eq. (1):

$$f_c = -\left(\frac{\varepsilon_c}{\varepsilon_{cp}}\right) f_{cp} \frac{n}{n-1+\left(\frac{\varepsilon_c}{\varepsilon_{cp}}\right)^{nk}} \tag{1}$$

where ε_{cp} represents the strain at peak stress f_{cp} while n is a parameter to adjust the pre-peak behavior and k a parameter to adjust the post-peak behavior, both of which depend on the value of f_{cp}. The event of unloading is modeled using Ramsberg-Osgood formulation and reloading follows a linear function up to the last unloading point. Fig. 5a shows a scheme of this behavior.

Under tension, concrete fracture is progressive, thus the bearing capacity of the material is reduced as the crack opening evolves, which is usually carried out using a softening function [23]. In this case, a smeared crack model is adopted, so the fracture behavior is reproduced at the material level and the softening function is expressed in terms of stresses and strains. Although more sophisticated functions can be used for the backbone curve in the tension domain, such as exponential or bilinear functions, it is usually enough to use a linear function, which is the option used here, following Eq. (2):

$$f_t = f_{tp}\left[1 - \frac{\varepsilon_t - \varepsilon_{tp}}{\varepsilon_{th} - \varepsilon_{tp}}\right] \geq 0 \tag{2}$$

where f_t represents the stress at strain ε_t, ε_{tp} represents the strain at the maximum strength f_{tp} and ε_{th} is the strain at which the material loses all its bearing capacity, as can be observed in Fig. 5b. This diagram is defined by only two parameters, which describe the fracture behavior of a quasi-brittle material like concrete, f_{tp} and the fracture energy G_f. As in the case of the material behavior under compression, unloading follows Ramsberg-Osgood formulation and reloading is linear.

Crack width is computed as $w = \varepsilon_{t1} s_{cr1}$ where ε_{t1} is the principal concrete tensile strain and s_{cr1} the distance used to compute the crack width. In this case, since the crack opening is parallel to the sleeper longitudinal axis and a regular mesh is used where elements are oriented with it, s_{cr1} coincides with the element side.

4. Mechanical behavior of sleepers for the fastening of the rails

Once the MMPC sleepers are accurately positioned on the ballasted railway track, the rails are then fastened by applying a tightening torque, T, to the screws that fix the SKL-1 elastic clips to the rail base. Each screw is therefore subjected to a tension axial force, N_s, when it is

Table 1
Properties of the materials.

Material	f_{cp} (N/mm^2)	f_{tp} (N/mm^2)	E (N/mm^2)	ν	α (°C^{-1})	t (mm)
Concrete (HP−60-C)	60	4.05	34,694	0.20	$6{\cdot}10^{-6}$	-
Concrete (HP−60-S)	60	4.05	34,694	0.20	$12{\cdot}10^{-6}$	-
Prestressed steel	1335	1335	200,000	0.30	$10{\cdot}10^{-6}$	-
Steel (screw)	500	500	200,000	0.30	$10{\cdot}10^{-6}$	-
Dowel-D2	70	70	3200	0.39	$100{\cdot}10^{-6}$	4.6
Dowel-D3	120	120	11,000	0.39	$100{\cdot}10^{-6}$	4.6

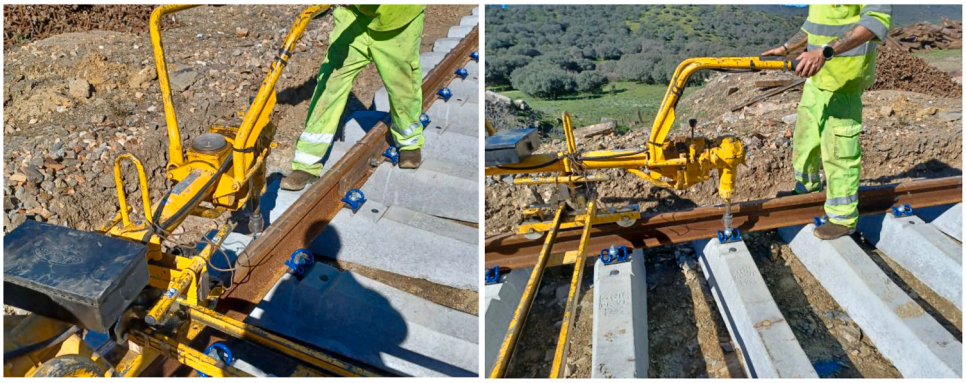

(a) (b)

Fig. 10. Fastening of the rails to the MMPC sleeper: (a) exterior screw; (b) interior screw.

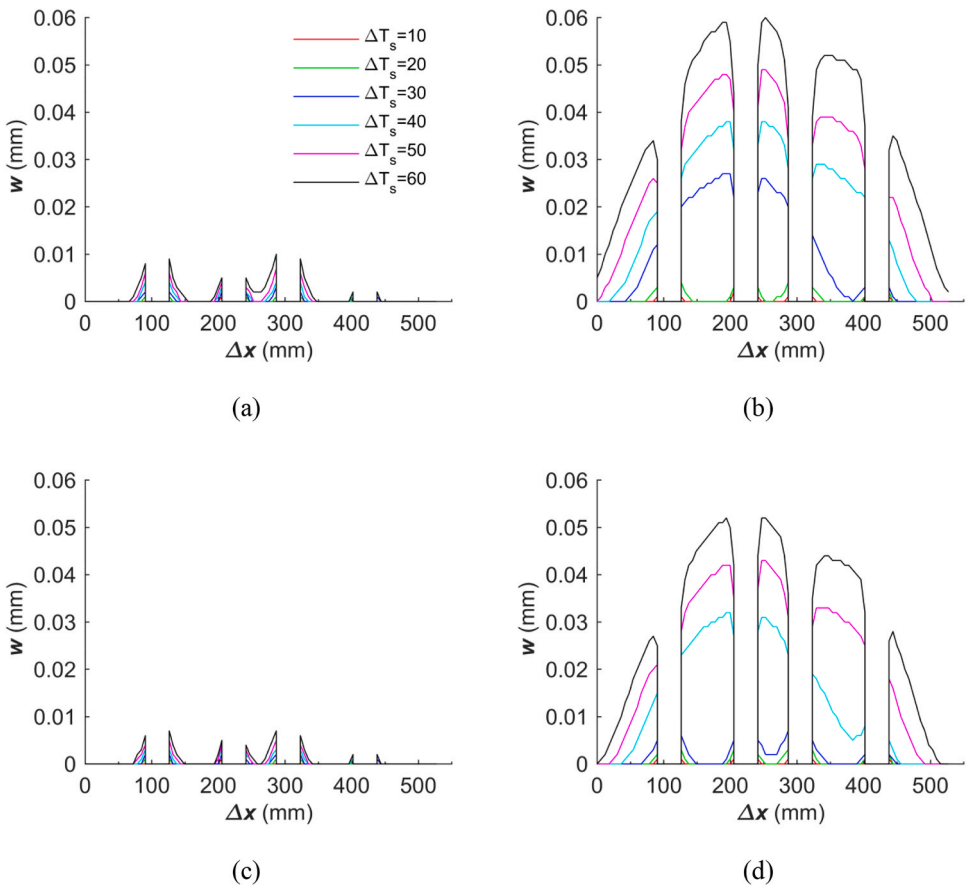

Fig. 11. Crack opening profile at the Z_i-zones for stockpiled sleepers: (a) CD2; (b) CD3; (c) SD2; (d) SD3.

eventually fixed between the dowel and the elastic clip SKL-1. The relationship between T and N_s for a screw installed in the fastening system can be expressed using the well-known formula [24]:

$$T = KN_s\phi_{M,s} \tag{3}$$

where $\phi_{M,s}$ is the major diameter of the screw thread and K is the torque coefficient that should be experimentally determined. The latter relies on the geometry of screws and washers as well as the coefficients of friction between screws and both washers and dowels, respectively [24].

4.1. Experimental test for assessing the torque coefficient for the SKL fastening system

No references in the literature provide the coefficient of friction between zinc-plated screws and polyamide dowels, nor the torque coefficient K of the screw in the SKL fastening system. Therefore, an experimental test was conducted at the Construction Engineering Laboratory of the University of Jaén to determine K, also considering the aging of SKL-1 clips and screws. Two clip-screw sets were studied: the first one—Set-U—was previously used and installed in a sleeper stockpiled outdoors for several months while the second one—Set-Un—was unused and, therefore, unaffected by both a previous fastening torque and the outdoors conditions.

Fig. 6a and b show the set-up for both tests where the red SKL-1 clip belongs to Set-U and the blue one to Set-Un. Both fastening systems were installed in the MMPC sleeper to fix a portion of a rail track (UIC-54) supported on an elastic seat pad. The lab equipment consisted of: (i) a digital torque wrench with a capacity up to 800 Nm and a 21 × 28 mm torque wrench socket for 1″ square drive; (ii), the software to record the torque sequence data; (iii) two dial displacement gauges—digital and analog—with a resolution of 0.01 mm (Fig. 6). The digital (DG) and the analogic (AG) dial gauges measured the vertical displacement of the SKL-1 clip and the vertical displacement of the rail, respectively (Fig. 6). The SKL-1 clip is a deformed steel bar with two different parts: a flexible—movable—part directly stressed by the screw and the rest of the clip that provides four simple supports. Since two legs of the clip are supported on the rail base (Fig. 6c and d), the displacements displayed by DG result from the combined deformation of the flexible part of the clip and the settlement of the seat pad under the rail.

The target tightening torque was set to 280 Nm, exceeding the 220 Nm required by the Spanish railway infrastructure manager (ADIF) for fastening the rails to MMPC sleepers equipped with the SKL fastening system [25]. This torque was applied using a digital torque wrench in a sequence of 21 stages, with 10 Nm increments per stage up to $T = 160$ Nm, followed by 20 Nm increments until reaching the target torque. Fig. 7a and b illustrate the cumulative torque and their corresponding vertical displacements, v, for Set-U and Set-Un, respectively. Three lines depict T with different vertical displacements: those measured by DG and AG, and their difference identified with DG-AG. The latter represents the relative vertical displacement between the end of the flexible part and the simple support parts of the SKL-1 clip, $v_{e,clip}$.

Moreover, the lines for DG and $v_{e,clip}$ show two different regions. The first one lies for the torque values that range from 0 up to 180 Nm, and represents the elastic clip deforming freely until it contacts the guide plate at $v_{e,clip} = 10$ mm. From this point, a steeper second region is obtained until reaching $T = 280$ Nm at $v_{e,clip}$ about 11 mm where the elastic clip and the guide plate are in contact. It can be observed that T is 10–20 Nm higher for Set-Un than the obtained for Set-U when $v_{e,clip}$ ranges between 1 mm and 8 mm that corresponds to T values of 10 Nm and 160 Nm, respectively. Once the clip touches the guide plate ($v_{e,clip} \geq$ 10 mm), the T-$v_{e,clip}$ relationship becomes consistent between the two sets.

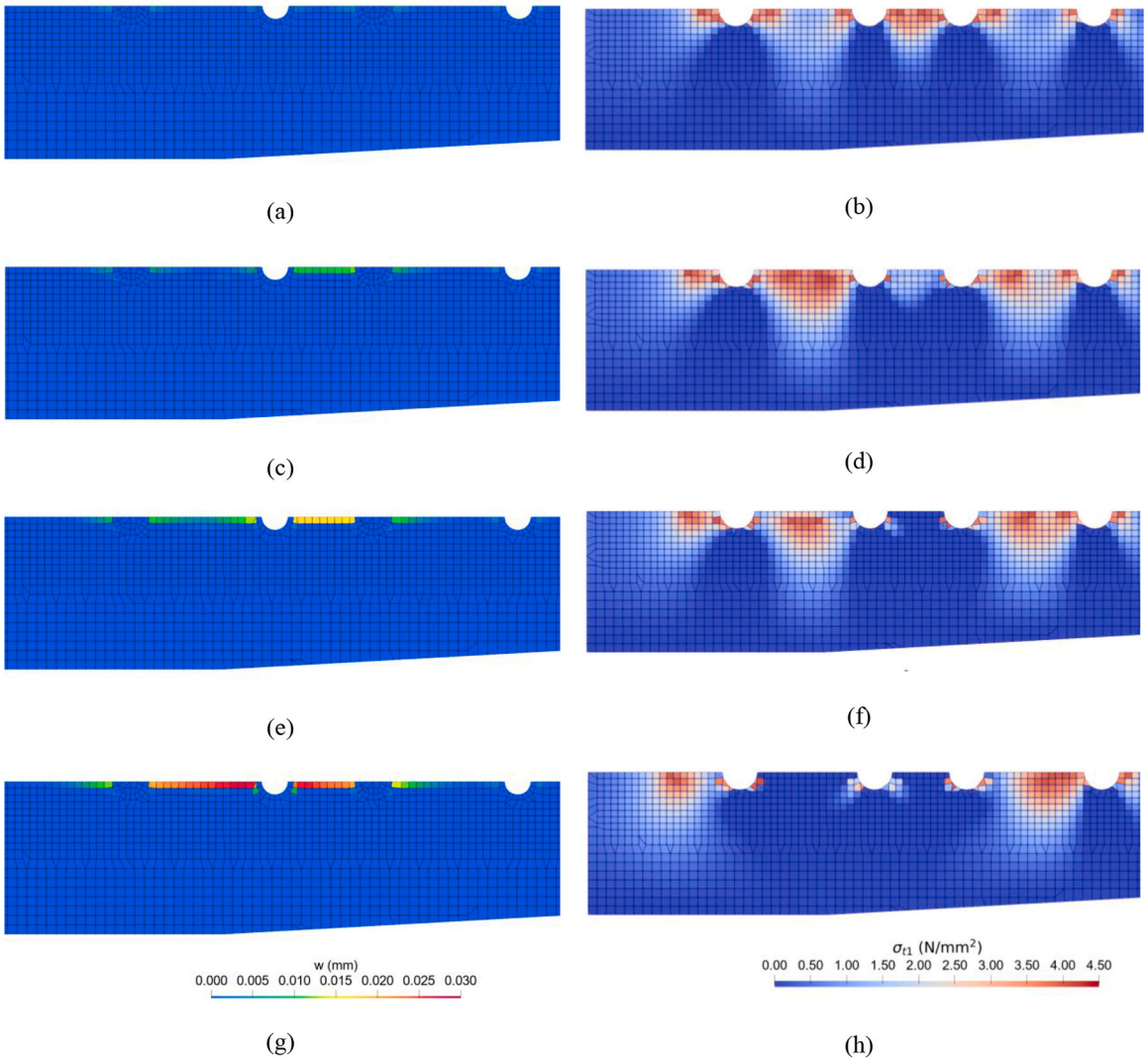

Fig. 12. Crack opening (left column) and principal concrete tensile stress (right column) for CD3 stockpiled at different temperatures: $\Delta T_s = 20$ ℃ (a and b); $\Delta T_s = 28$ ℃ (c and d); $\Delta T_s = 29$ ℃ (e and f); $\Delta T_s = 30$ ℃ (g and h).

There are different relationships in the literature that relate the force applied on the clip, F, and the vertical deformation of the flexible part of the elastic clip SKL-1, v_{clip}. Fig. 7c shows two approaches proposed by Ferrero et al. [26] from the Laboratory of Science and Engineering Materials at the University of Cantabria (LADICIM) and ADIF [27], both obtained from experimental tests of the elastic clip without guides plates. Both approaches considered the vertical displacement of the flexible part of the elastic clip but applied at different locations (Fig. 6d): the first one at the end, $v_{e,clip}$, as defined previously, and the second one at the center, aligned with the screw axis, $v_{s,clip}$. Both of them matches until the vertical displacement is $v_{clip} = 6$ mm, but they diverge beyond this point due to the increased deformation at the end of the flexible part. Hence, the LADICIM approach is used to determine the axial force transmitted from the elastic clip to the screw for $v_{e,clip} \leq 10$ mm, for which, the elastic clip moves freely without contacting the guide plate. When the clip is installed on the SKL fastening system, F is the axial force of the screw under tightening torque, that is, $F = N_s$. Consequently, the relationship between T and N_s is established using both the T- $v_{e,clip}$ data obtained experimentally and the N_s-$v_{e,clip}$ relationship proposed by LADICIM for $v_{e,clip}$ ranging between 0 and 10 mm (Fig. 7d). Additionally, the linear least-squares fit for each T-N_s dataset is depicted in Fig. 7d. The coefficient of determination and the slope of the fitting analysis were $R^2 = 0.99$ and $m = 23.36$ mm, respectively, for both Set-U and Set-Un. Therefore, K can be estimated using Eq. (3) as $K = m/\phi_{M,s} = 1.06$. This value is relatively high for the friction coefficient of the fastening system compared to values obtained in screwing joints used in mechanical applications [24]. This phenomenon can be attributed to the combined effect at two contact zones: the zinc plated washer with the painted elastic clip and the zinc plated screw with the polyamide dowel. The y-intercept of the least-squares linear regression for Set-U and Set-Un were −3.45 and 7.70, respectively. Then, for the sake of simplicity the relationship between T and N_s will be linear with $m = 23.36$ mm and y-intercept = 0, falling within the range obtained with Set-U and Set-Un.

4.2. Assessment of stresses generated by the fastening system in the sleeper

The polyamide dowels considered in this work are of the helical-thread type, characterized by oblique helicoidal surfaces with flat crests (Fig. 8). The tightening torque applied to the screw generates stresses within the dowel which are then transmitted to the surrounding concrete. This stress field depends on the geometry of the dowel's thread. Accordingly, a local reference system is defined at a generic point on the external surface of the thread to determine the stress components (Fig. 8a): the Z-axis aligns with the dowel's longitudinal axis; the X-axis is radial and the Y-axis is determined by the cross product of the X and the

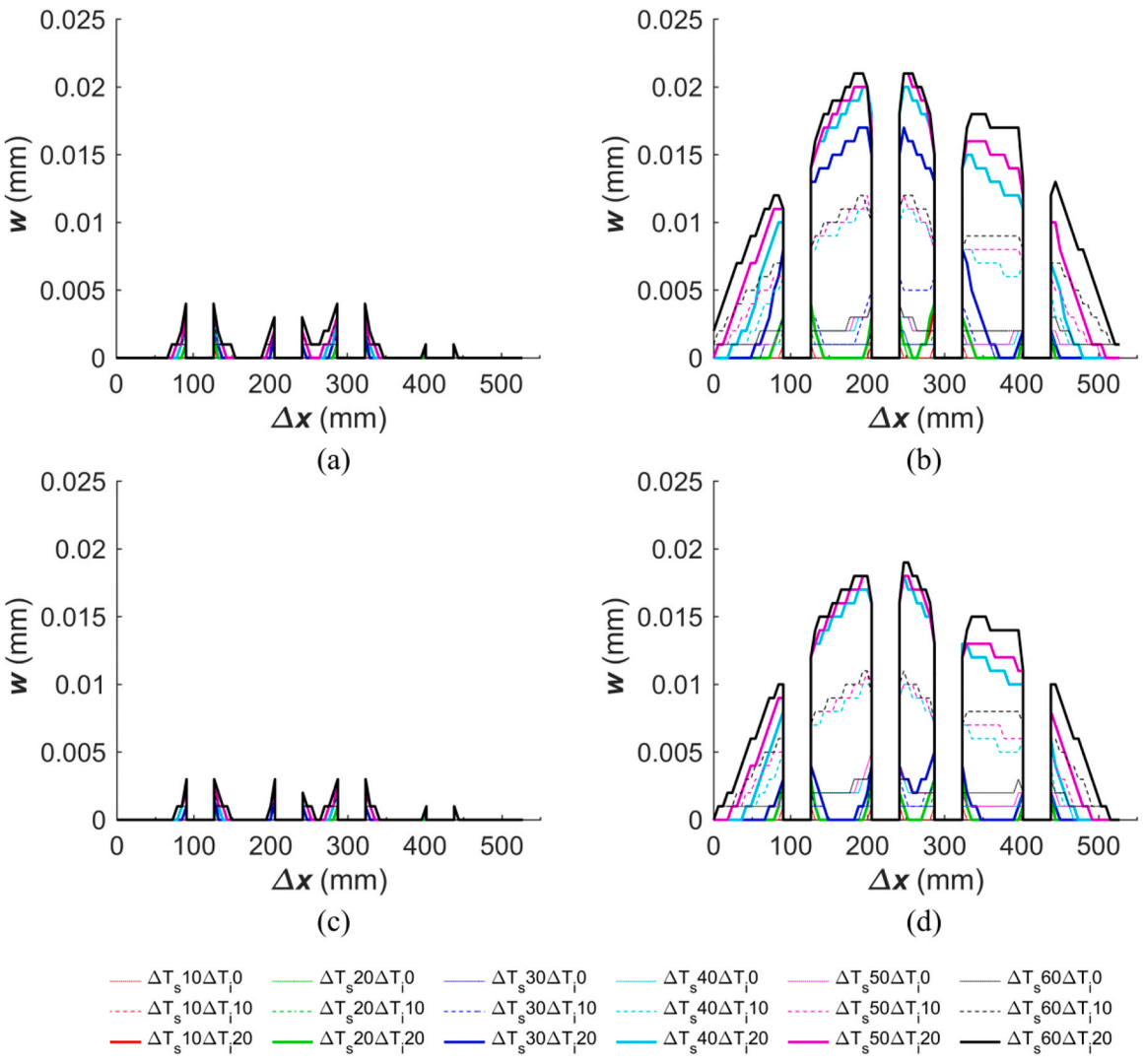

Fig. 13. Crack opening profile at the Z_i-zones for sleepers under the neutralization temperature: (a) CD2; (b) CD3; (c) SD2; (d) SD3.

Z axes. The lead angle is denoted by λ (Fig. 8b) and half of the thread angle is denoted by θ (Fig. 8c). The tangent plane (Fig. 8a) is defined by vectors **a** and **b**, where the former is the unit vector tangent to the helical-thread (Fig. 8b) and the latter is the unit vector aligned with the direction defined by the thread angle (Fig. 8c).

Thus, vectors **a** and **b** are defined as $\boldsymbol{a} = -\cos\lambda\mathbf{j} - \sin\lambda\mathbf{k}$ and $\mathbf{b} = \cos\theta\mathbf{i} - \sin\theta\mathbf{k}$, where **i, j** and **k** are the unit vectors of the reference system's canonical base. The normal vector of the tangent plane, **n** (Fig. 8a), is defined by $\mathbf{n} = \mathbf{a}\mathbf{x}\mathbf{b} = (\sin\theta\cdot\cos\lambda)\mathbf{i} - (\cos\theta\cdot\sin\lambda)\mathbf{j} + (\cos\lambda\cos\theta)\mathbf{k}$, where **n** is also a unit vector, and its components are the direction cosines expressed as $n_x = \cos a$, $n_y = \cos b$ and $n_z = \cos c$.

The stress transmitted by the dowel-screw set to the surrounding concrete, σ, is assumed to be perpendicular to the tangent plane defined above and, therefore, aligned with **n**. It is defined as follows. First, its vertical component (Fig. 8d) is calculated as $\sigma_v = N_s/S_{tot}$, where S_{tot} is the total area of the dowel's helicoidal surface. Then, $\sigma = \sigma_v/\cos c = N_s/(S_{tot}\cos\lambda\cos\theta)$. Finally, the radial component of the stress vector—along X axis—is determined as follows (Fig. 8d):

$$\sigma_r = \sigma\cos a = \frac{N_s}{S_{tot}}\tan\theta \tag{4}$$

On the other hand, the numerical model employs a 2D-FEM with a plain external surface for the dowel. Then, the radial compression stress applied to the dowel in the 2D-FEM which produces the same resultant force as the actual dowel (Fig. 9), is obtained as follows:

$$\sigma_{r,eq} = \frac{\sigma_r S_{tot}}{\pi\phi_{M,d}l_d} \tag{5}$$

where $\phi_{M,d}$ and l_d are the major diameter and the total length of the dowel, respectively.

Furthermore, the reaction stress exerted by the pinned support on the symmetry axis over the dowel in the 2D-FEM is also $\sigma_{r,eq}$. Consequently, the reaction force of one-half of the dowel-screw set at the sleeper`s longitudinal axis, R_{Torque}, subjected to the uniform radial stress $\sigma_{r,eq}$ (Fig. 9) is estimated using Eqs. (3), (4) and (5) as follows:

$$R_{Torque} = \sigma_{r,eq}\phi_{M,d}l_d = \frac{\sigma_r S_{tot}}{\pi} = \frac{T}{K\phi_{M,s}\pi}\tan\theta \tag{6}$$

4.3. Equivalent temperature-based model for the torque in the 2D-FEM of the sleeper

The compressive stresses in the concrete surrounding the dowel, caused by the tightening torque, can be indirectly estimated in the sleeper's 2D-FEM by applying an equivalent temperature increment to both the screw, $\Delta T_{eq,s}$ and the dowel, $\Delta T_{eq,d}$. The goal is for this effect to produce a reaction force in the dowel-screw set, R_{FEM}, that matches the R_{Torque} obtained from Eq. (6). R_{FEM} is calculated in the 2D-FEM by

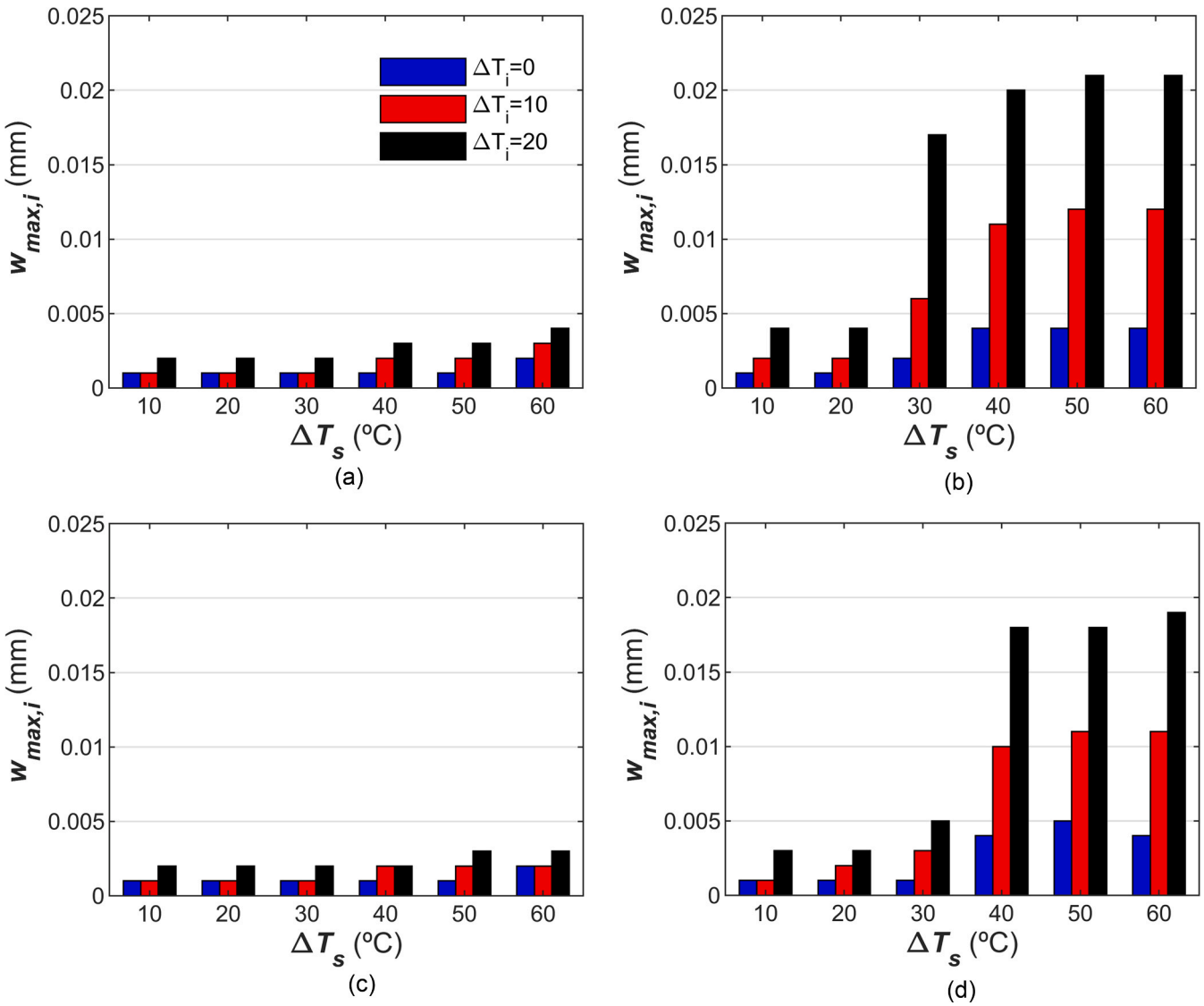

Fig. 14. Maximum crack opening for sleepers under the neutralization temperature: (a) CD2; (b) CD3; (c) SD2; (d) SD3.

summing the contributions of the reaction forces of the dowel and the screw. Since the dowel and the screw have different thermal expansion coefficients—α_d and α_s, respectively—and to ensure a homogeneous volume change of the dowel-screw set that accurately simulates the stresses field caused by the torque in the surrounding concrete, the temperature increments applied to the dowel, $\Delta T_{eq,d}$, and the screw, $\Delta T_{eq,s}$, are related by expression $\Delta T_{eq,d} = \Delta T_{eq,s}\alpha_s/\alpha_d$.

To estimate the effect of fastening the screw to the sleeper in a nonlinear model, a $R_{FEM} - \Delta T_{eq,s}$ relationship is convenient to determine $\Delta T_{eq,s}$—and subsequently $\Delta T_{eq,d}$— to be applied to the dowel-screw set in the 2D-FEM such that $R_{FEM} = R_{Torque}$. The following procedure was employed to obtain this relationship:

1. A load case was created in the 2D-FEM to apply temperature increments to the selected dowel-screw set, simulating a torque higher than the expected. Then, a total temperature increment of 75 °C was applied to the screw in 15 stages—5 °C per stage— to improve the analysis convergence. For the dowel, the corresponding temperature increment per stage was 5 α_s/α_d °C, as explained previously.
2. $R_{FEM,i}$ was calculated for the i-th stage, and then, the $R_{FEM} - \Delta T_{eq,s}$ relationship was then obtained.

Thus, the effects of any value of T applied to the sleeper can be estimated as follows. First, R_{Torque} is calculated from Eq. (6). Second, $\Delta T_{eq,s}$ is obtained from the $R_{FEM} - \Delta T_{eq,s}$ relationship. Third, $\Delta T_{eq,d}$ is calculated from $\Delta T_{eq,s}$. Finally, the nonlinear analysis of the 2D-FEM is performed by applying both $\Delta T_{eq,s}$ and $\Delta T_{eq,d}$ to the screw and the dowel, respectively.

5. Numerical simulations of the entire sleeper installation process

To simulate the sleeper installation process, the following conditions to represent each stage are described:

1. Fabrication. The fabrication temperature, T_f, corresponds to the ambient temperature after the sleepers are removed from the heating and curing chamber. This research considers three different values for T_f, 10, 20 and 30 °C, representing the fabrication of sleepers in winter, spring and summer, respectively. The total prestressed load applied to the sleeper was 450 kN (112.5 kN per wire). Furthermore, the shrinkage and the creep of concrete are omitted in the analysis due to the low long-term shortening allowed for MMPC sleepers (< 0.05 %) [28].

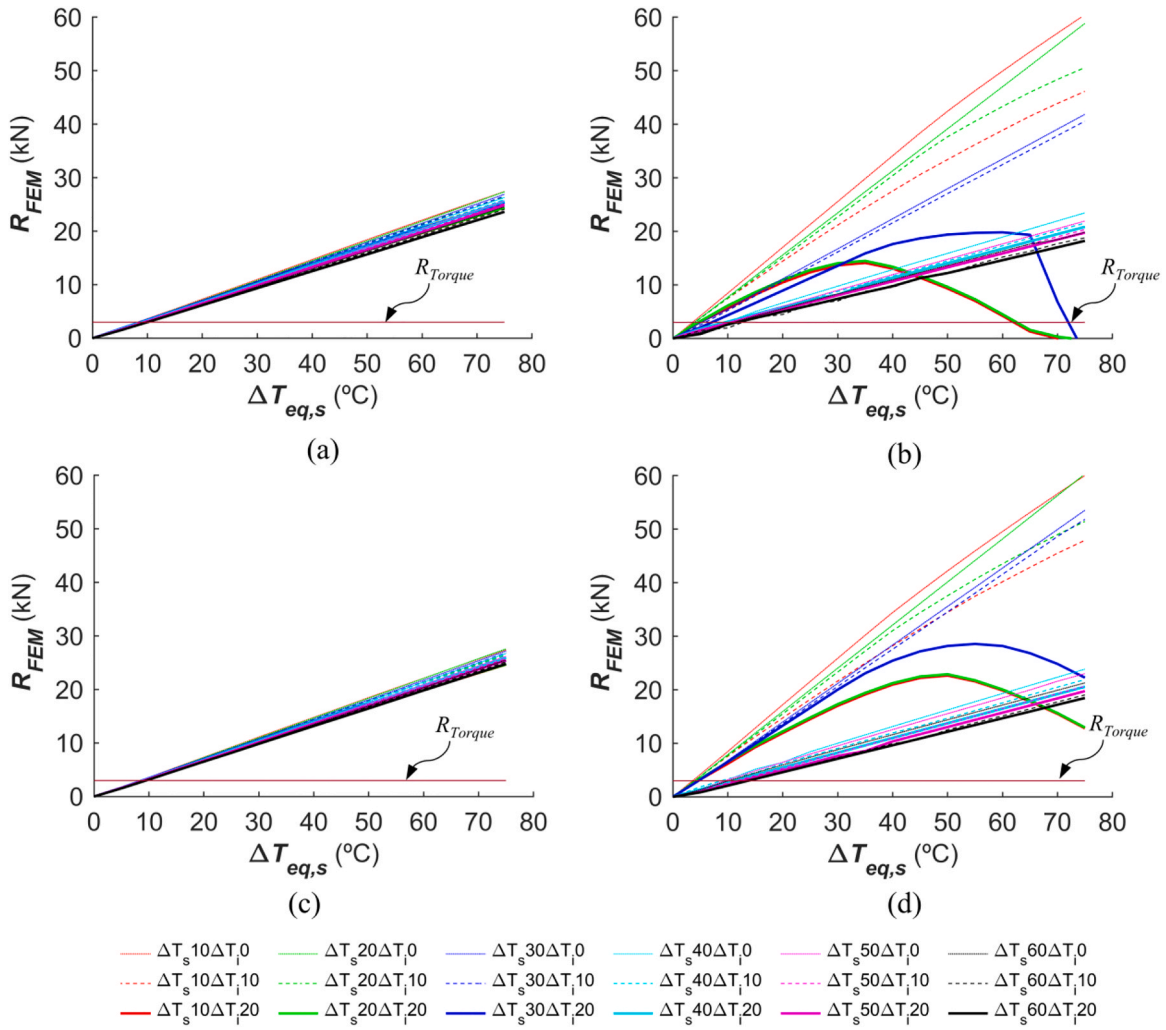

Fig. 15. $R_{FEM} - \Delta T_{eq,s}$ relationships for the dowel-screw system No. 2: (a) CD2; (b) CD3; (c) SD2; (d) SD3.

2. Stockpiling and placement alongside the track. The sleeper temperature can reach $T_f + \Delta T_s$. Six temperature levels are considered for ΔT_s: 10, 20, 30, 40, 50 and 60 °C, representing a range from neutral to extreme outdoor temperatures, following the criterion established in a previous study [16]. On the other hand, the sleepers are stacked before transportation using vertically aligned wooden spacers between them, placed outside the fastening system area, transmitting vertical compression stresses. As a result, the influence of these stresses on longitudinal crack opening is considered negligible and is therefore disregarded in this study.
3. Installation on the track and neutralization of continuous welded rails. After installation on the ballast, the rails are laid on the sleepers without fastening. The neutralization process is carried out through solar heating, allowing the ambient temperature to reach the neutralization temperature, T_n. At this point, the temperature of the sleepers, T_i, is considered equal to T_n. In this study, T_n is set to 30 °C. Since $T_i = T_n = T_f + \Delta T_i$, ΔT_i can be 0, 10 and 20 °C for sleepers fabricated in summer, spring and winter, respectively. The temperature variation relative to the previous stage—stockpiling— is $\Delta T_{is} = \Delta T_i - \Delta T_s$, which can be positive or negative.
4. Fastening the rails. The required tightening torque, $T_r = 220$ Nm [25], is applied to the screws to fasten the neutralized rails to the sleepers. Following standard practice (Fig. 10), the screws are fastened alternately for each rail. In this study, the interior screw (No. 2) is fastened first, followed by the exterior screw (No. 1).

Furthermore, this study considers the influence of concrete and dowel types commonly used in the prefabricated sleeper industry. Two types of concrete are considered, distinguished by the aggregate used in their fabrication: carbonate (C) and siliceous (S). Both types exhibit the same mechanical properties and follow the same constitutive model, except for the thermal expansion coefficient, which differs due to the aggregate type. For the dowels, two types are considered: low-modulus polyamide (D2) and high-modulus glass-fiber reinforced polyamide with 35 % glass-fiber (D3). The dowel numbering used in a previous study [16] is maintained here. The dowel thickness, t, refers to the main body of the dowel. Sleeper models are identified by (i) aggregate type and (ii) dowel material. For example, SD2 denotes a sleeper with siliceous aggregate concrete and a D2 dowel. Table 1 reports the properties of the different materials used in the analysis, where E is the elastic modulus, ν the Poisson's ratio and α the thermal expansion coefficient [16].

Four numerical models were created by varying the aggregate type (C and S) and the dowel material (D2 and D3). A series of nonlinear evaluations were conducted, considering the different conditions at each stage of the process, from the fabrication to the rail installation. Each calculation consisted of five load cases: (i) prestress load at T_f (fabrication); (ii) ΔT_s (stockpiling); (iii) ΔT_{is} to reach T_i (sleeper installation and rail neutralization); (iv) fastening of the screw No. 2; (v) fastening of the screw No. 1. The tightening torque applied to each dowel-screw set was estimated using equivalent temperature increments obtained from the $R_{FEM} - \Delta T_{eq,s}$ relationships, as described in Section 4.3. For the analysis of the tightening torque applied to the screw No. 2, the $R_{FEM} - \Delta T_{eq,s}$

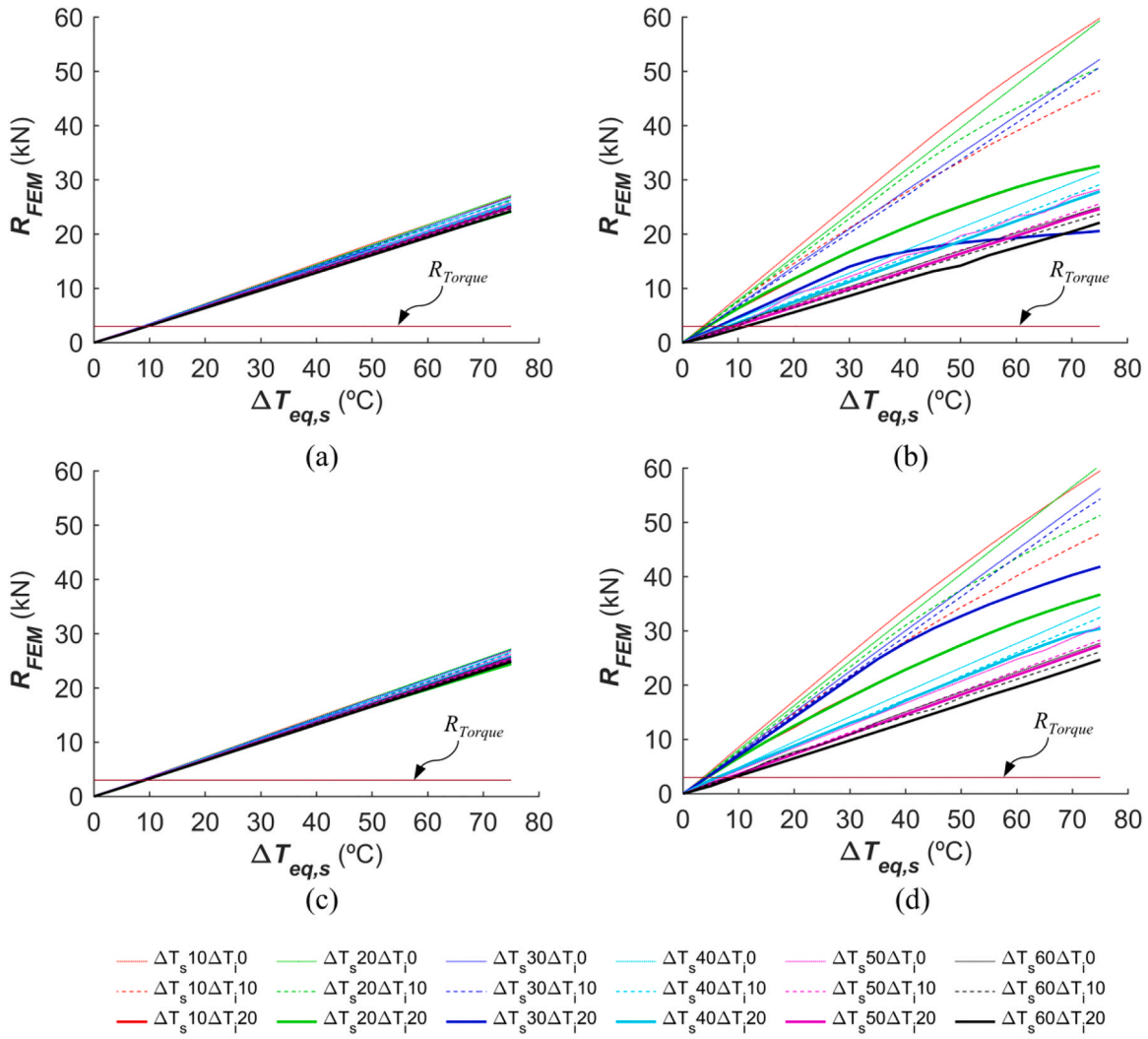

Fig. 16. $R_{FEM} - \Delta T_{eq,s}$ relationships for the dowel-screw system No. 1: (a) CD2; (b) CD3; (c) SD2; (d) SD3.

relationship was obtained after applying the first three load cases. Then, the equivalent temperatures $\Delta T_{eq,s2}$ and $\Delta T_{eq,d2}$ were determined, along with the sleeper's response under these conditions. Next, for the fastening of the screw No. 1, a new analysis was performed using the same procedure, but considering the initial stress and strain conditions obtained at the end of screw No. 2 fastening load case. This yielded $\Delta T_{eq,s1}$ and $\Delta T_{eq,d1}$, and hence, the sleeper's behavior under the tightening torque applied to the screw No. 1.

Therefore, a total of 72 nonlinear numerical evaluations were conducted in Vector2 [20], accounting for the four numerical models, the six levels of ΔT_s and the three levels of ΔT_i.

6. Cracking analysis of MMPC sleepers

This study focused on analyzing longitudinal cracks initiated in the longitudinal strip where the dowels are located, specifically at the Z_i-zones (Fig. 4). The analysis of crack opening and propagation is conducted for the different stages of the MMPC sleeper installation process, considering the varying outdoors temperature conditions proposed in Section 5.

6.1. Fabrication

The sleepers are prestressed, exhibiting an elastic behavior with absence of cracking except to the anchorage zone of the prestressed bars. In this stage concrete does not reach the tensile limit of 4.05 MPa.

6.2. Sleepers stockpiled and placed alongside the track

Sleepers can reach high temperatures during this process, particularly in summer. Fig. 11 illustrates the crack opening, w, at the different Z_i-zones (see Fig. 4), during the stockpiling stage. D2-sleepers—sleepers fabricated with dowel D2—exhibited slight cracking (Fig. 11a and c), without significant increments of ΔT_s. Up to $\Delta T_s = 30$ °C, the maximum crack opening was $w = 0.004$ mm and $w = 0.003$ mm in sleepers made with carbonate and siliceous aggregates, respectively. In the temperature range of 40 °C $\leq \Delta T_s \leq$ 60 °C there is a significant increase in the maximum w, ranging between 0.007 mm and 0.01 mm with carbonate aggregates and between 0.005 mm and 0.007 mm with siliceous aggregate.

For D3-sleepers with carbonate aggregate, a sharp increase in w is observed between $\Delta T_s = 20$ °C and 30 °C (Fig. 11b). At $\Delta T_s = 20$ °C, the maximum crack opening was $w = 0.004$ mm. From this point onwards, w increased significantly reaching a maximum of $w = 0.027$ mm at $\Delta T_s = 30$ °C —seven times the previous value, 0.038 mm at $\Delta T_s = 40$ °C and even 0.06 mm at $\Delta T_s = 60$ °C. A similar trend was observed with siliceous aggregate (Fig. 11d) for ΔT_s ranging between 30 °C and 40 °C. In both cases, a brittle failure occurred, starting in Z3 and propagating to Z4 and Z2. Fig. 12 shows the sequence for CD3 (left column) along with the corresponding principal concrete tensile stress levels, σ_{t1} (right

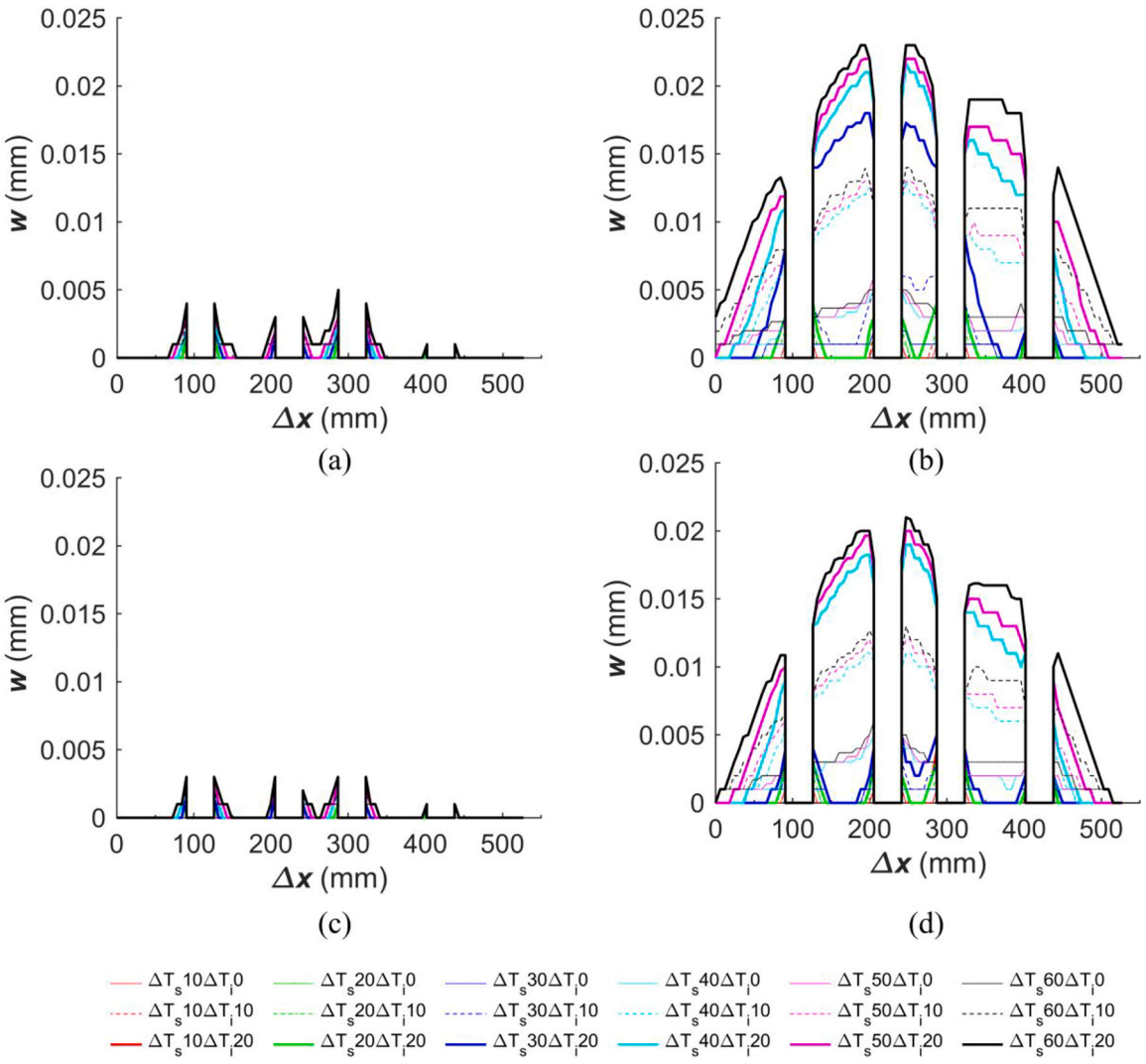

Fig. 17. Crack opening profile at the Z_i-zones for sleepers after rails fastening: (a) CD2; (b) CD3; (c) SD2; (d) SD3.

column), from $\Delta T_s = 20$ ℃ to $\Delta T_s = 30$ ℃. For low values of w (Fig. 12a and c), σ_{t1} retains non-zero values in the Zi-zones (Fig. 12b and d). Nevertheless, for larger values of w (Fig. 12e and g), such as in the Z2 and Z3 zones, ε_{t1} occurs within the strain softening region of the constitutive model (Fig. 5b), causing σ_{t1} to approach zero (Fig. 12f and h). For the siliceous aggregate model, the brittle failure occurred at $\Delta T_s = 34$ ℃. Therefore, D3-sleepers fabricated in winter and stockpiled or placed near the track for installation in summer are more susceptible to damage, especially those made with carbonate aggregate.

Regarding the different types of concrete aggregates, it is observed that, overall, sleepers with siliceous aggregates exhibit lower cracking levels than those with carbonate aggregates. Specifically, the maximum crack opening for D2-sleepers with siliceous aggregate is, on average, 100 % and 70 % of that observed with carbonate aggregates for $\Delta T_s \leq 20$ ℃ and $\Delta T_s > 20$ ℃, respectively. For D3-sleepers these differences reach 60 % and 90 % for $\Delta T_s \leq 20$ ℃ and $\Delta T_s > 30$ ℃, respectively. In the case of $\Delta T_s = 30$ ℃, the sleeper with carbonate aggregate experiences brittle failure, unlike the one with siliceous aggregate, and hence, the maximum crack opening for the latter is 25 % of the former.

6.3. Installation of the sleepers on the track and neutralization of the rails

The sleepers, previously stockpiled, are then installed on the railway track at T_n, allowing the rails to move freely over them. The analysis considered three levels of temperature increment over fabrication, ΔT_i, for rail neutralization: 0, 10 and 20 °C. Fig. 13 illustrates the values of w reached at the Z_i-zones of the sleeper for this stage, where dotted, dashed and solid lines correspond to ΔT_i values of 0, 10 and 20 °C, respectively. In all models, the maximum crack opening, $w_{max,i}$, takes place always in Zones 2 or 3.

When $T_i \leq T_s$, Fig. 14 shows that $w_{max,i}$ is lower than the maximum crack opening obtained for the sleepers stockpiled, $w_{max,s}$ (Fig. 11), especially for ΔT_i equal to 0 and 10 °C. For D2-sleepers, the cracking is limited to values around half of $w_{max,s}$ (lower than 0.005 mm). For D3-models, a different behavior is observed depending on ΔT_i. For $\Delta T_i = 0$, the cracking level is similar to that observed in D2-sleepers, regardless of the stockpiling temperature. The same trend was observed for $\Delta T_i > 0$ and ΔT_s limited to 20 °C and 30 °C for sleepers with carbonate and siliceous aggregates, respectively. Nevertheless, sleepers for $\Delta T_i > 0$ and ΔT_s exceeding those limits exhibit higher cracking levels, between two and four times that obtained with $\Delta T_i = 0$, showing less crack opening recovery.

On the other hand, it is worth to emphasize that the differences in maximum crack opening between sleepers with different aggregate types when $\Delta T_i > 0$ follow the same trend observed in the stockpiling stage. Nevertheless, for $\Delta T_i = 0$ there are no apparent differences between them.

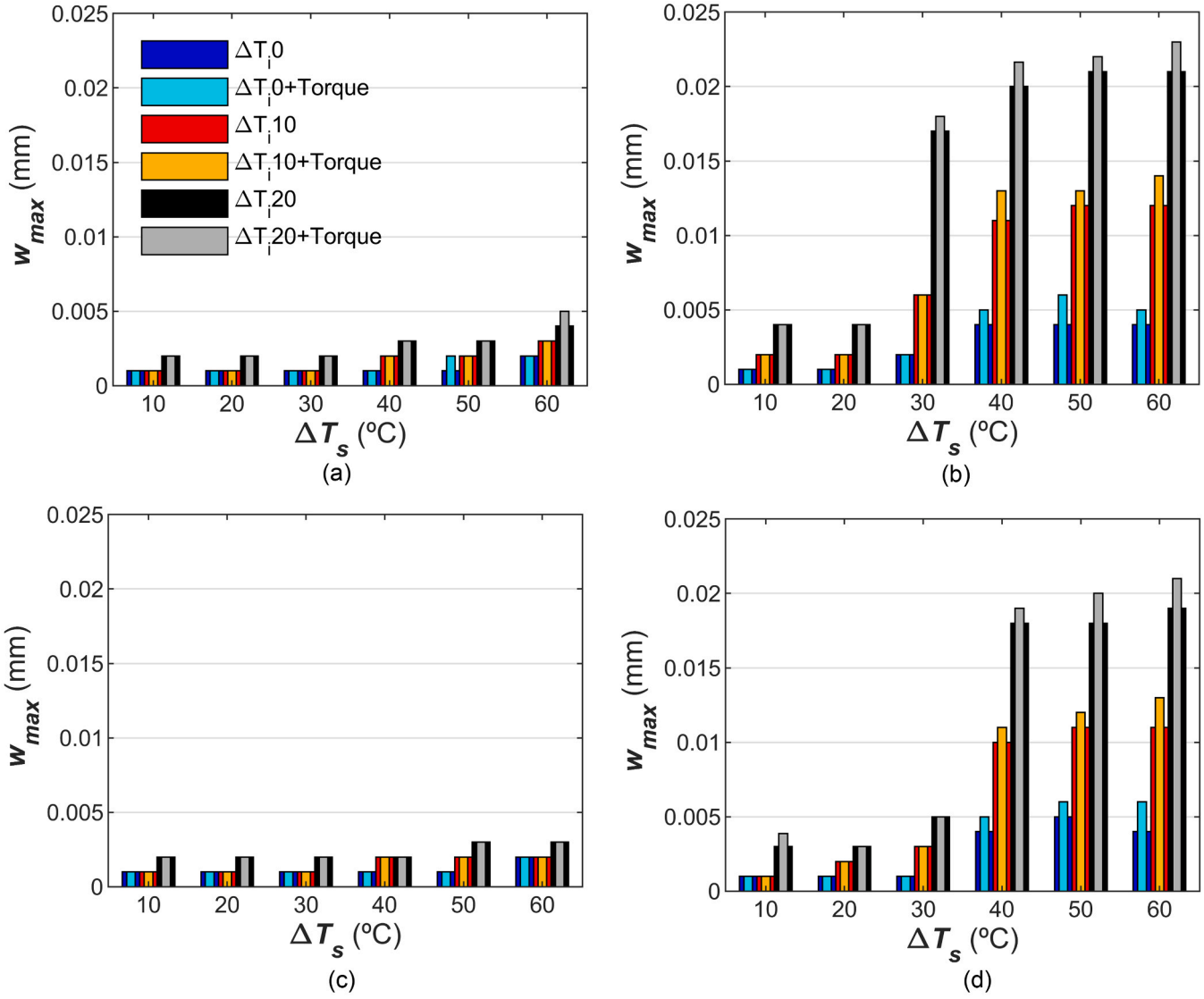

Fig. 18. Maximum crack opening after rails fastening compared to the track installation stage: (a) CD2; (b) CD3; (c) SD2; (d) SD3.

6.4. Fastening of the rails

The rails are fastened to the sleepers after neutralization, by applying the torque $T_r = 220$ Nm alternately to each screw. This action generates a reaction force on each dowel-screw system determined by the Eq. (6), resulting in $R_{Torque} = 3.00$ kN for $K = 1.06$, $\phi_{M,s} = 22$ mm and $\theta = 45°$. The equivalent temperature-based model was applied on each dowel-screw set to obtain the $R_{FEM} - \Delta T_{eq,s}$ relationships for the different models under various ΔT_s and ΔT_i conditions considered in the analysis. Fig. 15 and Fig. 16 illustrate these relationships for the dowel-screw No. 2 and No. 1, respectively. A horizontal line represents the required reaction force R_{Torque} generated by T_r. The intersection of this line with each $R_{FEM} - \Delta T_{eq,s}$ curve determines $\Delta T_{eq,s2}$ and $\Delta T_{eq,s1}$ which are used to study the influence of the torque applied to the screws No. 2 and No. 1, respectively.

Fig. 15 and Fig. 16 also show that, in all cases, T_r was effectively applied to both screws No. 1 and No. 2. Given that $R_{Torque} = 3.00$ kN for $T_r = 220$ Nm, there is a large safety margin (at least 5 times T_r) for accidental values of the fastening torque, as $R_v \geq 15$ kN for all $R_{v,FEM} - \Delta T_{eq,s}$ relationships.

On the other hand, it is worth noting that $R_{FEM} - \Delta T_{eq,s}$ relationship reflects the capacity of the dowel-screw-concrete joint to absorb the torque action. D2-sleepers exhibit a very stable capacity regardless of the applied $\Delta T_{eq,s}$ (Fig. 15a and c, Fig. 16a and c). Only a slight variation in the slope of the $R_{FEM} - \Delta T_{eq,s}$ relationships is observed with increasing ΔT_s and ΔT_i. This is due to the low cracking opening and the absence of the crack propagation along the dowel strip in the sleeper. Nevertheless, D3-sleepers show a different behavior. At $\Delta T_s \leq 30$ °C the capacity degradation was observed at $\Delta T_i = 20$ °C, consistent with the higher cracking opening—between two and three times greater—than that observed for lower levels of ΔT_i (Fig. 14b and d). For $\Delta T_s > 30$ °C, the curves are less steep, indicating a reduced capacity compared to lower ΔT_s values, with significantly higher crack openings and apparent crack propagation. The slope was similar to that obtained with D2-sleepers, but the underlying causes differ: cracking of the surrounding concrete in D3-sleepers and the lower elastic modulus of the dowel in D2-sleepers.

Fig. 17 shows the crack opening in sleepers after the rails have been fully fastened, that is, when $\Delta T_{eq,s}$ and $\Delta T_{eq,d}$ are applied to the dowel-screw systems No. 2 and No. 1, respectively. The differences in the crack pattern between sleepers fabricated with siliceous and carbonate aggregates follow the same trend as observed in the previous stage—sleeper installation and rail neutralization.

Fig. 18 shows the change in the maximum crack opening at this stage compared to that reached at the installation stage. For D2-sleepers (Fig. 18a and c), the changes are negligible. For D3-sleepers (Fig. 18b

and d), the increments range between 0.001 mm and 0.003 mm for $\Delta T_s \geq 30$ ℃ in sleepers with carbonate aggregate and for $\Delta T_s \geq 40$ ℃ in those with silicious aggregate. Therefore, sleepers stockpiled with $\Delta T_s \geq 30$ ℃ are prone to experiencing increased crack openings when they are fabricated with D3 dowels.

7. Conclusions

This study analyzed the effects of thermal and mechanical loads on the longitudinal cracking of monoblock multipurpose prestressed concrete (MMPC) sleepers throughout their fabrication, stockpiling, installation with rail neutralization and fastening of the rails. A validated 2-D numerical model of the sleeper was used to simulate the evolution of longitudinal cracks in the dowel area where the SKL fastening system are located using non-linear evaluations. Different thermal conditions were considered during the fabrication, stockpiling and installation, with ΔT_s and ΔT_i representing temperature differences from fabrication for the stockpiling and installation, respectively. The prestress load during fabrication and the tightening torque applied to the screws during rail fastening were also considered. An equivalent temperature model was applied to each screw-dowel set to replicate the effects of the tightening torque on concrete. Various materials used in sleeper fabrication were considered, including different types of concrete aggregates (carbonate and siliceous) and dowels (low-modulus polyamide and high-modulus glass-fiber reinforced polyamide). The following conclusions can be drawn:

1. **Torque Coefficient**: SKL fastening systems have a higher torque coefficient K = 1.06—tightening torque and screw axial force relation—than typical screwed joints.
2. **Dowel Stiffness and Cracking**: low-modulus polyamide dowels exhibit less cracking than glass-fiber reinforced polyamide dowels, despite having the same thermal expansion.
3. **Sleeper Performance**: sleepers with low-modulus polyamide dowels remain stable in all stages, with minimal cracking.
4. **Glass-Fiber Dowel Brittleness**: sleepers with glass-fiber dowels are prone to cracking, especially when they are fabricated under cold conditions and then stockpiled and installed on the railway track in warm conditions. This can lead to significant crack propagation.
5. **Tightening Torque**: sleepers with low-modulus polyamide dowels retain their torque capacity under varying temperatures, while those with glass-fiber dowels may experience a significant reduction. Nevertheless, in all cases, they maintain a safety factor greater than 5 relatives to the required torque (220 kN).
6. **Cracking and Torque**: Applying tightening torque to sleepers with glass-fiber dowels and stockpiled with $\Delta T_s \geq 30$ ℃ can exacerbate existing cracks.
7. **Concrete Impact**: Sleepers with siliceous aggregate concrete exhibit lower crack openings than those with carbonate aggregate concrete, particularly during stockpiling (between 10 % and 40 % reduction for $\Delta T_s \geq 20$ ℃). This trend persists during installation and fastening.

CRediT authorship contribution statement

Jesús Donaire Ávila: Writing – original draft, Project administration, Methodology, Investigation, Formal analysis, Conceptualization. **Javier F. Aceituno:** Writing – review & editing, Validation, Supervision, Resources, Investigation. **Fernando Suárez:** Writing – review & editing, Validation, Software.

Declaration of Competing Interest

The authors declare that they have no known competing financial interests or personal relationships that could have appeared to influence the work reported in this paper.

Acknowledgements

The authors gratefully acknowledge the financial support provided by the Ministry of Science, Innovation and Universities of Spain through the Research Fund Project PID2023-149321OA-C33. The authors also express their gratitude to the sleeper manufacturer Andaluza de Traviesas S.A. for providing essential information on the manufacturing and stockpiling processes of sleepers.

Data availability

Data will be made available on request.

References

[1] Janeliukstis R, Clark A, Papaelias M, Kaewunruen S. Flexural cracking-induced acoustic emission peak frequency shift in railway prestressed concrete sleepers. Eng Struct 2019;178:493–505. https://doi.org/10.1016/j.engstruct.2018.10.058.
[2] You R, Kaewunruen S. Evaluation of remaining fatigue life of concrete sleeper based on field loading conditions. Eng Fail Anal 2019;105:70–86. https://doi.org/10.1016/j.engfailanal.2019.06.086.
[3] Theogene N. Optimization of concrete sleepers subjected to static and impact loadings. Eng Perspect 2021;3:92–8. https://doi.org/10.29228/eng.pers.52117.
[4] Kaewunruen Sakdiratand, Akono Ange-Theres, Remennikov Alex M. Attenuation effect of material damping on impact vibration responses of railway concrete sleepers. In: El-Badawy Sherif, Valentin J, editors. In: Proceedings of the second GeoMEast international congress and exhibition on sustainable civil infrastructures. Sustainable solutions for railways and transportation engineering. Cham (Egypt): Springer International Publishing; 2019. p. 98–107.
[5] Sol-Sánchez M, Moreno-Navarro F, Rubio-Gámez MC. The use of elastic elements in railway tracks: a state of the art review. Constr Build Mater 2015;75:293–305. https://doi.org/10.1016/j.conbuildmat.2014.11.027.
[6] Indraratna B, Qi Y, Tawk M, Heitor A, Rujikiatkamjorn C, Navaratnarajah SK. Advances in ground improvement using waste materials for transportation infrastructure. Proc Inst Civ Eng - Ground Improv 2022;175:3–22. https://doi.org/10.1680/jgrim.20.00007.
[7] Qiang W, Jing G, Connolly DP, Aela P. The use of recycled rubber in ballasted railway tracks: a review. J Clean Prod 2023;420. https://doi.org/10.1016/j.jclepro.2023.138339.
[8] Jing G, yunchang D, You R, Siahkouhi M. Comparison study of crack propagation in rubberized and conventional prestressed concrete sleepers using digital image correlation. Proc Inst Mech Eng F J Rail Rapid Transit 2022;236:350–61. https://doi.org/10.1177/09544097211020595.
[9] Kaewunruen S, Li D, Chen Y, Xiang Z. Enhancement of dynamic damping in eco-friendly railway concrete sleepers using waste-tyre crumb rubber. Materials 2018;11. https://doi.org/10.3390/ma11071169.
[10] Ferdous W, Manalo A. Failures of mainline railway sleepers and suggested remedies – review of current practice. Eng Fail Anal 2014;44:17–35. https://doi.org/10.1016/j.engfailanal.2014.04.020.
[11] de Souza Lima EH, Pereira Carneiro AM. A review of failures of railway monoblock prestressed concrete sleepers. Eng Fail Anal 2022;137:106389. https://doi.org/10.1016/j.engfailanal.2022.106389.
[12] Kaewunruen S, Fu H, Ye C. Numerical studies to evaluate crack propagation behaviour of prestressed concrete railway sleepers. Eng Fail Anal 2022;131:105888. https://doi.org/10.1016/j.engfailanal.2021.105888.
[13] César Bastos J, Dersch MS, Edwards JR. Degradation mechanisms of concrete due to water flow in cracks of prestressed railroad sleepers under cyclic loading. J Mater Civ Eng 2022;34. https://doi.org/10.1061/(ASCE)MT.1943-5533.0004144.
[14] Salahi Nezhad M, Floros D, Larsson F, Kabo E, Ekberg A. Numerical predictions of crack growth direction in a railhead under contact, bending and thermal loads. Eng Fract Mech 2022;261:108218. https://doi.org/10.1016/j.engfracmech.2021.108218.
[15] Tahi M, Chikhaoui M, Chabaat M. Analysis of cracking evolution mode of the monobloc sleeper. Int J Struct Integr 2023;14:435–57. https://doi.org/10.1108/IJSI-01-2023-0010.
[16] Donaire-Ávila J, Montañés-López A, Suárez F. Influence of temperature on the longitudinal cracking in multipurpose precast concrete sleepers prior to their installation. Materials 2019;12:9–11. https://doi.org/10.3390/ma12172731.
[17] Derkowski W, Ślaga. The effect of too stiff rail to base fastening on damage mechanism in RC ballastless track structure. Struct Concr 2020;21:1544–56. https://doi.org/10.1002/suco.201900366.
[18] Zeng Z, Peng G, Wang W, Huang X, Shen S, Shuaibu AA, et al. Research on the variable-temperature cracking mechanism of CRTS I type double-block ballastless track on a bridge. Materials 2022;15. https://doi.org/10.3390/ma15030770.
[19] ADIF [Spanish railway infrastructure manager]. NAV 7–1-4.1: Neutralización y Homogeniezación de Tensiones del Carril en la Vía Sin Juntas. Madrid; 2023.
[20] Wong PS, Vecchio FJ, Trommels H. Vector2 and FormWorks user's manual. Departament of Civil Engineering University of Toronto; 2002.
[21] Popovics S. A numerical approach to the complete stress-strain curve of concrete. Cem Concr Res 1973;3:583–99. https://doi.org/10.1016/0008-8846(73)90096-3.

[22] Thorenfeldt E, Tomaszewicz A, Jensen J. Mechanical properties of high strength concrete and application in design. In: Proceedings of the first international symposium on the utilization of high-strength concrete, Stavanger, Norway 1987: 149–59.
[23] Jirásek M. Damage and smeared crack models. In: Hofstetter Günter, Meschke G, editors. Numerical modeling of concrete cracking. Vienna: Springer Vienna; 2011. p. 1–49. https://doi.org/10.1007/978-3-7091-0897-0_1.
[24] Budynas RG, Nisbett JK. Shigley's mechanical engineering design. 10th edition. New York, USA: McGraw-Hill Education; 2015.
[25] ADIF (Spanish railway infrastructure manager). PAV 01_01.01.000_ED2: Sujeción VE - Características generales y componentes. Technical Regulations Database/ Normativa Técnica Vigente/Planos Tipo/01Sujeciones y Pequeño Material; 2024. Available from: ⟨https://normativatecnica.adif.es/ntw/⟩ [Accessed 30 October 2024].
[26] Ferreño D, Casado JA, Carrascal IA, Diego S, Ruiz E, Saiz M, et al. Experimental and finite element fatigue assessment of the spring clip of the SKL-1 railway fastening system. Eng Struct 2019;188:553–63. https://doi.org/10.1016/j.engstruct.2019.03.053.
[27] ADIF. E.T. 03.360.566.8: Technical specification for clips SKL-1. Madrid; 2022.
[28] ADIF. ET 03.360.571.8+M1: Traviesas monobloque de hormigón pretensado. Madrid: ADIF; 2024.